

Double-pulse streamer simulations for varying interpulse times in air

H Malla¹ , A Martinez^{1,2} , U Ebert^{1,2}  and J Teunissen^{1,*} 

¹ Centrum Wiskunde & Informatica (CWI), Amsterdam, The Netherlands

² Department of Applied Physics, Eindhoven University of Technology, PO Box 513, 5600 MB Eindhoven, The Netherlands

E-mail: jannis.teunissen@cw.nl

Received 23 February 2023, revised 27 July 2023

Accepted for publication 1 September 2023

Published 13 September 2023



CrossMark

Abstract

In this paper, we study how streamer discharges are influenced by a previous voltage pulse using an axisymmetric fluid model. We simulate double-pulse positive streamers in N₂–O₂ mixtures containing 20% and 10% O₂ at 1 bar. By varying the time between the pulses between 5 ns and 10 μs, we observe three regimes during the second pulse: streamer continuation, inhibited growth and streamer repetition. In the streamer continuation regime, a new streamer emerges from the tip of the previous one. In the inhibited regime, the previous channel is partially re-ionized, but there is considerably less field enhancement and almost no light emission. Finally, for the longest interpulse times, a new streamer forms that is similar to the first one. The remaining electron densities at which we observe streamer continuation agree with earlier experimental work. We introduce an estimate which relates streamer continuation to the dielectric relaxation time, the background field and the pulse duration. Furthermore, we show that for interpulse times above 100 ns several electron detachment reactions significantly slow down the decay of the electron density.

Keywords: streamer discharge, double pulse, streamer continuation, fluid model, electron detachment

(Some figures may appear in colour only in the online journal)

1. Introduction

Streamers are transient, filamentary gas discharges [1, 2]. Due to the strong electric field enhancement at their tips they can propagate in background electric fields below the breakdown threshold. In nature they occur as streamer coronas ahead of lightning leaders, and as tens of kilometers tall sprite discharges in the thin atmosphere high above thunderstorms. Streamer discharges can be used to generate various chemical species and they are used in applications such as plasma medicine [3–5], agriculture [6], industrial surface treatments [7], and combustion [8].

Streamers are commonly produced using a repetitively pulsed voltage source [9–11]. The repetition rate determines how strongly discharges are affected by previous pulses, through left-over ionized and neutral species as well as gas heating. Such effects from previous pulses can cause transitions between corona, glow and spark discharge regimes [12]. In [13], simulations were performed to study the evolution of electrons, positive and negative ions during the interpulse.

The effect of pulse repetition frequencies on positive streamers in molecular nitrogen-oxygen mixtures was studied systematically in double pulse experiments in [9, 10]. In [9] different formation and propagation behavior was observed for the second-pulse streamer depending on the time between the two voltage pulses. If this time was sufficiently short, the first-pulse streamers continued their growth during the second pulse. The maximum time between two voltage pulses for

* Author to whom any correspondence should be addressed.

which this happens was called the continuation time. The authors were able to explain how continuation times vary with the O₂ percentage by zero-dimensional plasma-chemical modeling.

The effect of previous pulses has also been analyzed experimentally or using global kinetics models in the context of plasma jets in [14, 15]. They focus on the minimum electron density needed to observe the repeatable behavior of a plasma jet. In a recent paper [16], three consecutive negative voltage pulses were simulated for an atmospheric plasma jet to investigate the role of left-over charged species after the first pulse. Repetitive-pulsed DBD experiments were performed in [17, 18], and different breakdown regimes were identified depending on the pulse-off time similar to [9]. Furthermore, streamer memory effects and discharge mode transitions due to repetitive pulses have been studied in a series of papers by Zhao *et al*, see e.g. [19, 20], and reviewed in [21].

The remaining electron density from a previous pulse can influence where a discharge will grow during the next pulse. Such an effect was observed [9], and it was studied in another context with laser-generated ionization in [22, 23]. The contribution of electrons detached from various negative ions to the seed electrons of subsequent pulses was studied in several papers [15, 16, 24, 25].

In this paper, we address an open question posed in [9]: which physical mechanism determines the electron density required for streamer continuation? Furthermore, we study how the second-pulse discharge changes when the time between the voltage pulses is increased beyond the continuation time. To this end, we perform simulations of double-pulse positive streamers in two N₂-O₂ mixtures with 20% and 10% O₂ at standard temperature and pressure, using a 2D axisymmetric fluid model. We use a detailed plasma chemistry including neutral and excited species, which allows us to investigate the relative contribution of various detachment reactions after the first pulse.

2. Model

We study streamer discharges at 1 bar and 300 K in two nitrogen-oxygen mixtures containing 20% and 10% oxygen in an average background field of 15 kV cm⁻¹. Axisymmetric simulations are performed with a standard drift-diffusion fluid model with the local field approximation, using the *afivo-streamer* code [26]. For a recent comparison of this model against experiments and against particle simulations see [27, 28]. We briefly summarize the main equations below, for further details see e.g. [26, 29].

2.1. Equations

The electron density n_e evolves in time as

$$\partial_t n_e = \nabla \cdot (\mu_e \mathbf{E} n_e + D_e \nabla n_e) + S_e + S_{ph}, \quad (1)$$

where μ_e is the electron mobility coefficient, D_e the diffusion coefficient, and \mathbf{E} the electric field. The electron transport coefficients are assumed to depend on the local electric

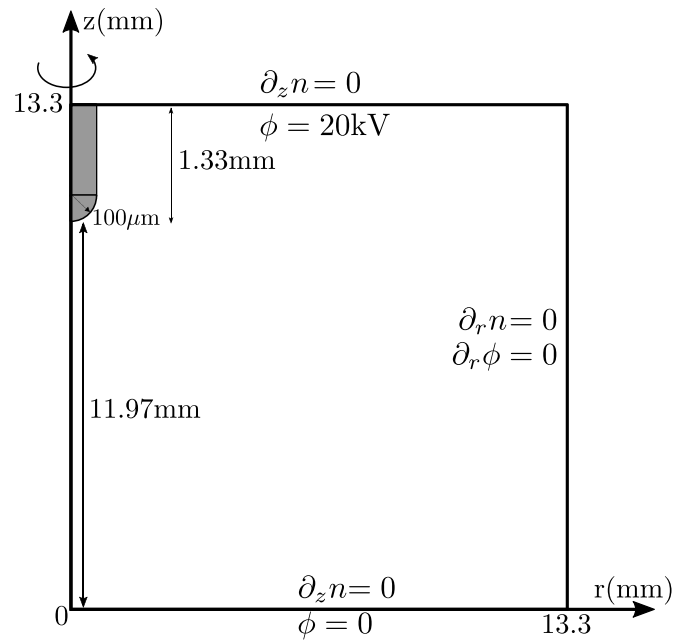


Figure 1. The axi-symmetric plate-plate geometry with a needle electrode. Boundary conditions for the species densities n and the electrostatic potential ϕ for each of the domain boundaries are given.

field (local field approximation) and were computed using BOLSIG- [30] using Phelps' cross-section data [31]. S_e is a source (and sink) term due to reactions involving electrons, for example ionization or attachment, see section 2.4. S_{ph} is a photo-ionization source term, which is here implemented according to Zhelezniak's model [32] as discussed in [29]. Ion and neutral densities n_i (numbered by $i = 1, \dots, n$) evolve in time as

$$\partial_t n_i + \nabla \cdot (q_i \mu_i \mathbf{E} n_i) = S_i. \quad (2)$$

Here S_i is a source/sink term due to reactions, μ_i is the mobility and q_i accounts for the species' charge (0 for neutrals, -1 for negative ions and $+1$ for positive ions).

The electric field \mathbf{E} is calculated in the electrostatic approximation as $\mathbf{E} = -\nabla \phi$. Here ϕ is the electrostatic potential, which is obtained by solving the Poisson equation [33, 34]

$$\nabla^2 \phi = -\rho / \epsilon_0, \quad (3)$$

where ρ is the space charge density and ϵ_0 is the vacuum permittivity.

2.2. Geometry

We use a plate-plate geometry with a needle electrode which is shown in figure 1. For species densities, homogeneous Neumann boundary conditions are used on all domain boundaries. For the electric potential, a homogeneous Neumann boundary is used on the outer radial boundary. The bottom plate is grounded, while a high voltage is on the upper plate and the needle electrode. The applied voltage is 20 kV, so that the average field between the plates is 15 kV cm⁻¹, which is about half the breakdown field at 1 bar.

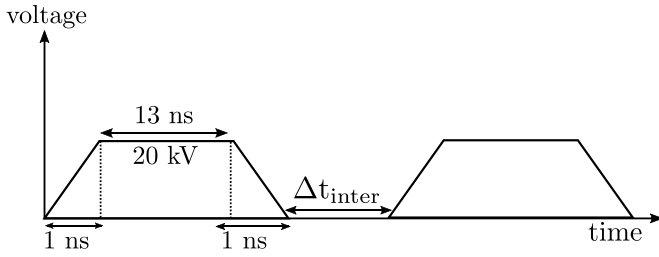


Figure 2. The applied voltage waveform with two identical pulses. The time between the pulses Δt_{inter} is varied from 5 ns to 10 μs .

Table 1. List of species used in the simulations. We use the reaction set described in [35].

Neutral	$\text{N}_2, \text{O}_2, \text{NO}, \text{NO}_2, \text{NO}_3, \text{N}_2\text{O}, \text{N}_2\text{O}_3, \text{N}_2\text{O}_5, \text{N}_2\text{O}_4, \text{O}_3, \text{N}(^4\text{S}), \text{N}(^2\text{D}), \text{N}(^2\text{P}), \text{O}(^1\text{D}), \text{O}(^1\text{S}), \text{O}(^3\text{P})$
Positive	$\text{N}^+, \text{N}_2^+, \text{N}_3^+, \text{N}_4^+, \text{N}_2\text{O}_2^+, \text{N}_2\text{O}^+, \text{NO}_2^+, \text{NO}^+, \text{O}_2^+, \text{O}_4^+, \text{O}^+$
Negative	$e^-, \text{N}_2\text{O}^-, \text{NO}_2^-, \text{NO}_3^-, \text{NO}^-, \text{O}_2^-, \text{O}_3^-, \text{O}_4^-, \text{O}^-$
Excited	$\text{N}_2(\text{rot}), \text{O}_2(\text{rot}), \text{N}_2(\text{A}), \text{N}_2(\text{B}), \text{N}_2(\text{a}), \text{N}_2(\text{C}), \text{N}_2(\text{E}), \text{O}_2(\text{a}), \text{O}_2(\text{b}), \text{O}_2(\text{A}), \text{N}_2(\text{v} = 1-8), \text{O}_2(\text{v} = 1-4)$

2.3. Voltage waveform and initial conditions

The applied voltage waveform is shown in figure 2, consisting of two identical pulses separated by a time Δt_{inter} that is varied from 5 ns to 10 μs . The peak voltage V_{appl} is 20 kV, which is applied during 13 ns, and the rise and fall times of the voltage are 1 ns. As an initial condition, we use a neutral (electrons and O_2^+) background ionization density of $1.8 \times 10^9 \text{ m}^{-3}$. This background ionization provides the first electrons for streamer inception near the electrode tip, where there is significant electric field enhancement. Inception occurs approximately 1 ns after the voltage is turned on.

2.4. Reaction set

We use the reaction set given in [35], containing 263 reactions, which was primarily compiled from the reactions given in [36, 37]. This set includes reactions between electrons, neutrals, ions, and excited species. A list of the 56 considered species is given in table 1. Rate constants for reactions involving electron collisions were computed with BOLSIG+ [30] using the cross-sections from [31]. We remark that the reaction set was designed for dry air (20% O_2 , 80% N_2), and that using the same reactions for 10% O_2 is an approximation as some rate coefficients could depend on the O_2 concentration.

We consider the motion of seven major ion species: N_2^+ , O_2^+ , N_4^+ , O_4^+ , O_2^- , O^- , and O_3^- ; other ions are assumed to be immobile. For simplicity, we assume that the mobile ions all have a constant mobility $2.2 \times 10^{-4} \text{ m}^2 \text{ V s}^{-1}$ [38], because ion motion played no major role for the results reported in this paper.

In section 4.4, we use the reaction set used in [39] which is a subset of the above described reaction set to demonstrate the effect of using a simplified reaction set on the interpulse plasma evolution.

3. Results

3.1. Effect of interpulse time on streamer continuation

We vary the interpulse time Δt_{inter} in two gas mixtures, consisting of N_2 with 20% O_2 or 10% O_2 , to study the properties of the streamer generated by the second voltage pulse. Figures 3 and 4 show streamers at the end of the second pulse (but before the voltage fall time) for varying Δt_{inter} , for the cases of 20% O_2 and 10% O_2 , respectively. In these figures, the instantaneous light emission is approximated by the Abel-transformed $\text{N}_2(\text{C}^3\Pi_u)$ density, since most of the emission comes from the second positive system [40]. The forward Abel transform was performed using the Hansen-Law method [41]. Axial electric field profiles corresponding to figure 3 are shown in figure 6.

Depending on Δt_{inter} , we observe three regimes: continuation, inhibited growth and streamer repetition, which are discussed below. In figure 5, we show the streamer evolution during the second pulse at equally spaced time intervals for $\Delta t_{\text{inter}} = 25 \text{ ns}$ and 50 ns.

3.1.1. Continuation regime. For short interpulse times the channel created by the first pulse still has a relatively high conductivity. The existing channel therefore becomes electrically screened during the second pulse, as shown in figure 5(a), leading to the emergence of a new streamer from its tip. For larger Δt_{inter} the conductivity of the existing channel is lower, which results in a longer electric screening time. This results in a longer inception delay for the second streamer, which is therefore shorter. The maximum time between the pulses for which continuation occurs is here called the streamer continuation time. In section 4.2 a criterion for streamer continuation is discussed.

3.1.2. Inhibited regime. For longer Δt_{inter} the first-pulse streamer channel has lost so much of its conductivity that it does not become fully screened during the second pulse (see figure 5(b)), and there is no streamer continuation. However, the electron density in the old channel is still high enough to inhibit a new streamer from forming, and a weak ionization wave passes through the channel instead. Light emission plots in figure 5 show that there is almost no light emission during the second pulse. In [9], such an inhibited regime was also observed. Other studies have also found that a relatively high background electron density reduces the field enhancement of a streamer, leading to slower discharge growth and a lower degree of ionization, see e.g. [23, 27].

3.1.3. Streamer repetition regime. For even longer Δt_{inter} , the re-ionization of the channel becomes more streamer-like,

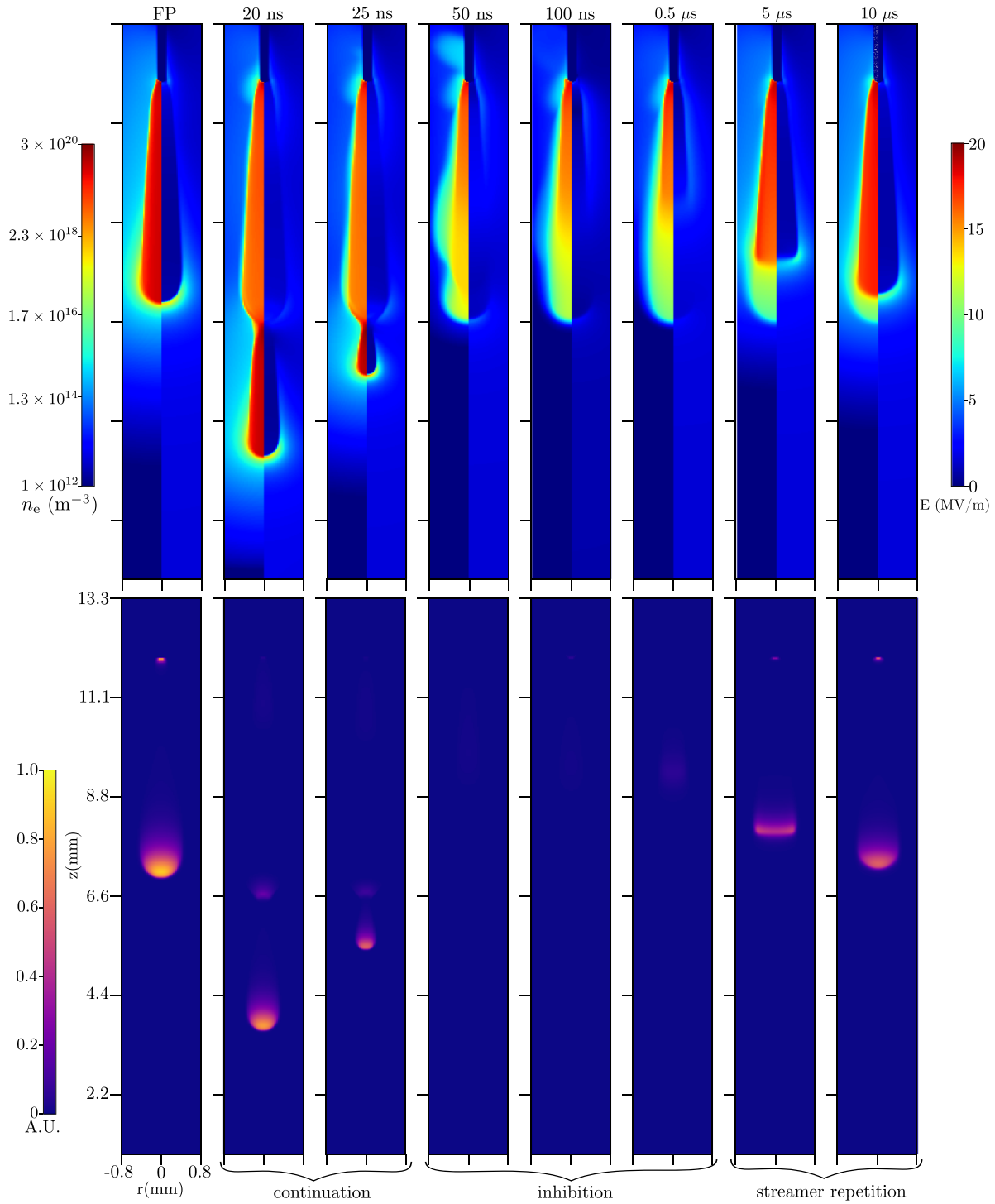


Figure 3. Plots of the first pulse (FP) streamer (left most column) and of the second streamer for interpulse times of 20 ns to 10 μ s (as indicated above each column), for 20% O₂. Each column shows electron density (top, left half) and electric field (top, right half) and instantaneous light emission (bottom), all at the end of the pulse but before the fall time. Light emission was computed using a forward Abel transform. The three observed regimes, streamer continuation, inhibited growth and streamer repetition are indicated.

as can be seen in figure 6: the electric field is enhanced at the tip of the re-ionized region and it is screened behind the tip. Note that the electric field for this second-pulse streamer is still weaker than for the first pulse, and that its head shape is somewhat deformed. Eventually, the electron density of the previous channel will become so low that it hardly affects the

evolution during the second pulse. We approach this behavior for $\Delta t_{inter} = 10 \mu$ s, where the second-pulse streamer therefore closely resembles the first-pulse streamer.

One might expect the effect of gas heating to influence the second-pulse streamer properties. However, this is not the case because the amount of energy deposited before the second

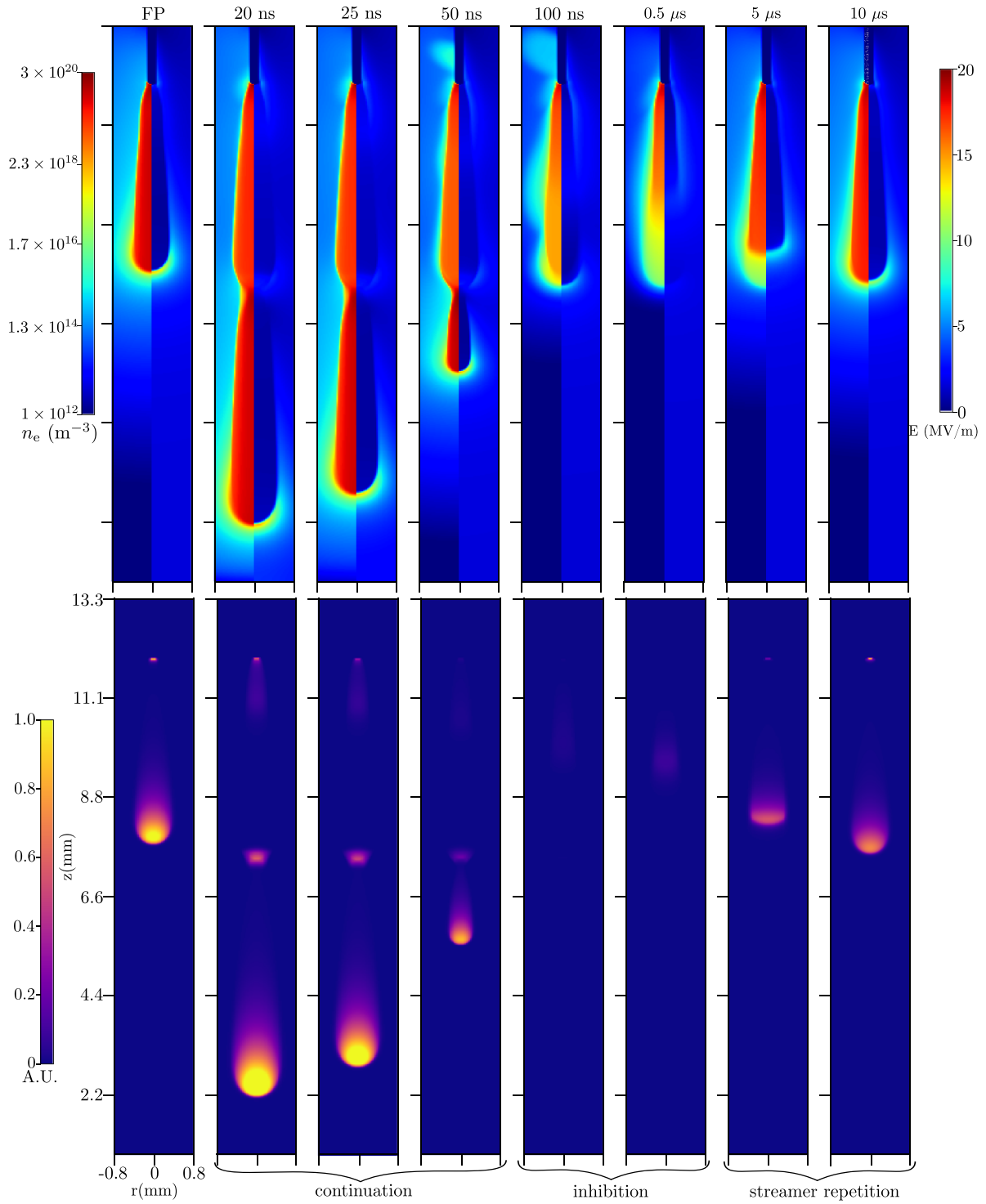


Figure 4. The same plots as in figure 3, but now for 10% O_2 .

pulse is so small that ambient gas heating is negligible, as discussed in appendix C.

3.2. Channel evolution between pulses

To better understand the evolution of second-pulse streamer, figure 7 shows the time evolution of the electron density at a point 1 mm below the electrode tip starting from

the moment when the first pulse is off, i.e. from $t = 15$ ns. We observe two electron decay timescales. For times up to $0.1 \mu s$, the electron density and hence the conductivity decay rapidly due to electron attachment and electron-recombination reactions. For $t > 0.1 \mu s$, the electron decay rate reduces due to detachment reactions. The main attachment and detachment reactions while the voltage is off are given in table 2.

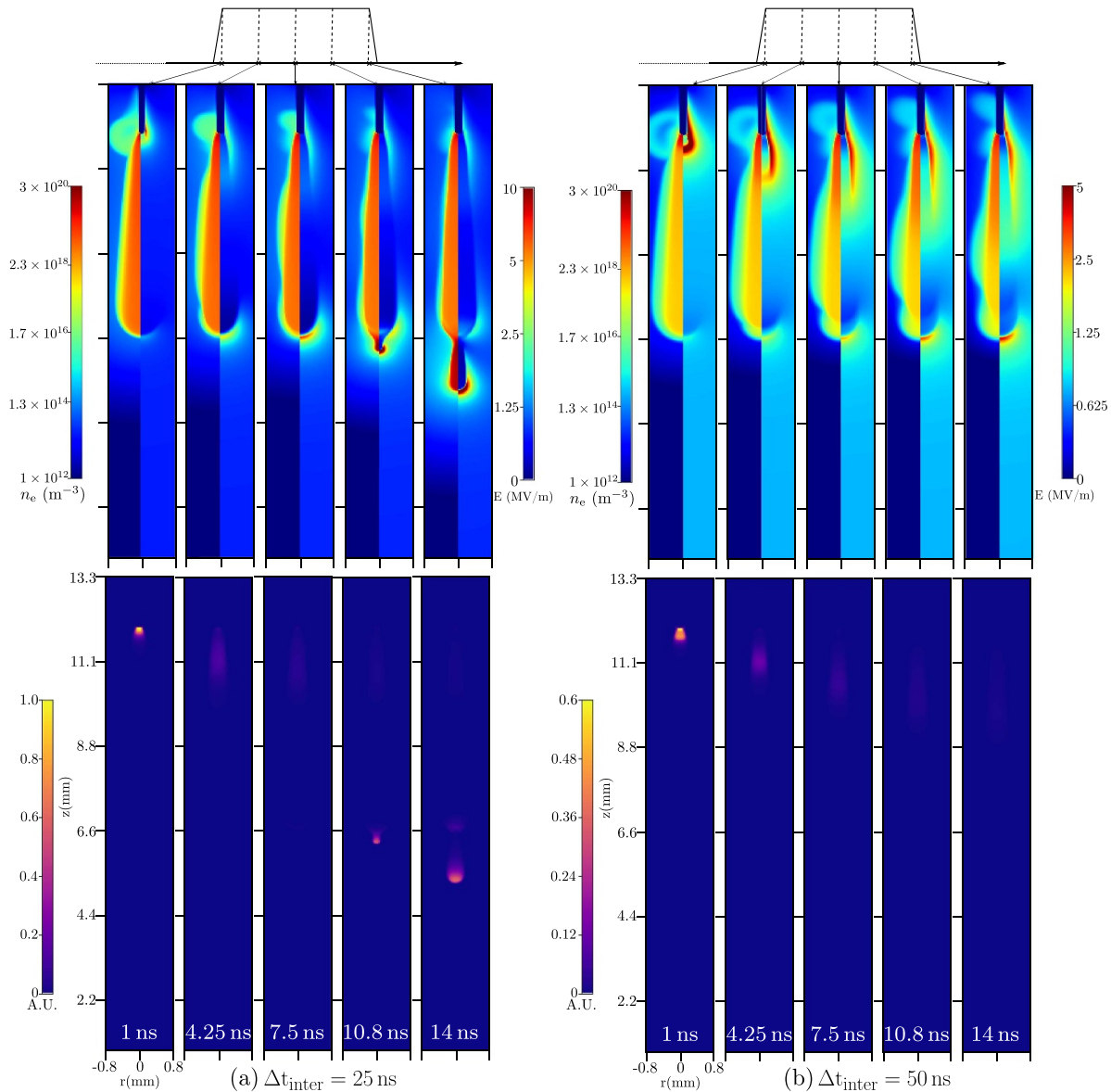


Figure 5. Evolution during the second voltage pulse for interpulse times of 25 and 50 ns, for 20% O₂, at equally spaced intervals. The time offsets with regard to the rise of the second voltage pulse are indicated at the bottom and visually at the top. On top, the electron density and the electric field are shown (left and right half of each image), and on the bottom the instantaneous light emission is shown.

The concentration of O₂ in the ambient gas mixture affects the relative contribution of different attachment reactions. For example, during an interpulse time of 500 ns, the percentage contribution to electron loss is as follows:

- Three-body attachment to O₂ gas (R1+R2): 75% (20% O₂) and 55% (10% O₂). Note that the rates of R1 and R2 depend quadratically and linearly on the O₂ concentration.
- Dissociative recombination (R3): 24% (20% O₂) and 44% (10% O₂). This reaction results from the fast conversion of positive ions into O₄⁺ inside the streamer channel [42].

Other reactions are responsible for only about 1% of the electron loss. These relative contributions are not sensitive to the interpulse time, with a variation of less than 10% for all the interpulse times.

4. Discussion

4.1. Comparison with earlier experimental work

In [22], double pulse streamer experiments were performed at 133 mbar for varying interpulse times and for varying O₂ concentrations. With 0D plasma-chemical modeling, it was estimated that the minimum remaining electron density n_e^{\min} for streamer continuation was about $5 \times 10^{17} \text{ m}^{-3}$, using a pulse duration t_{const} of about 200–300 ns with a rise/fall time of 15 ns. At 1 bar, these values scale to $n_e^{\min} \sim 3 \times 10^{19} \text{ m}^{-3}$ and $t_{\text{const}} \sim 27\text{--}30 \text{ ns}$, see [2].

For the simulations performed here, with a pulse duration $t_{\text{const}} \sim 13 \text{ ns}$, we observe streamer continuation for n_e^{\min} in the range of 10^{19} m^{-3} up to $4 \times 10^{19} \text{ m}^{-3}$. Compared to the results of [22], some deviations are to be expected, due the

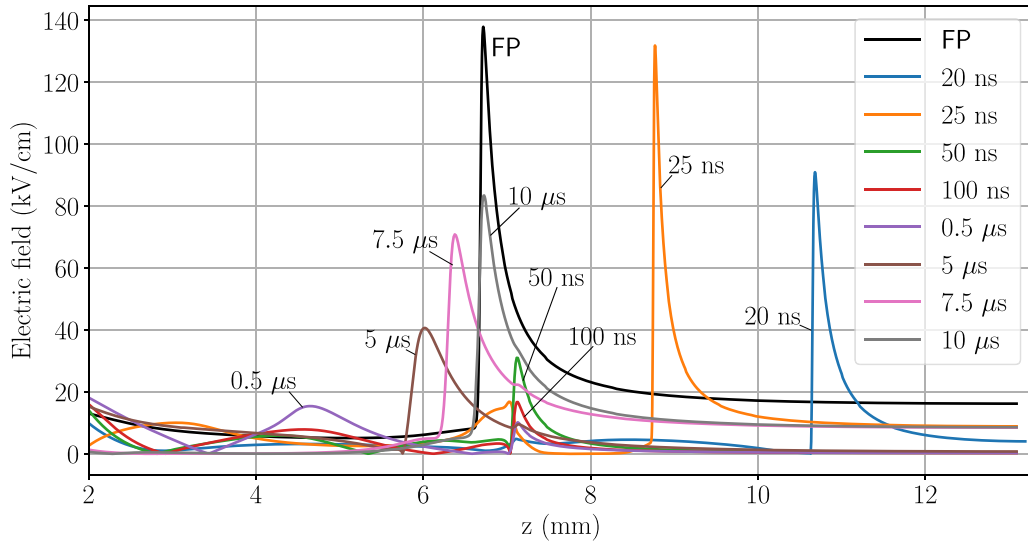


Figure 6. Electric field profile at the end of the second pulse (but before the voltage falls) for 20% O₂, at varying interpulse times. Electric field profile for the first-pulse streamer is plotted as a black curve for reference.

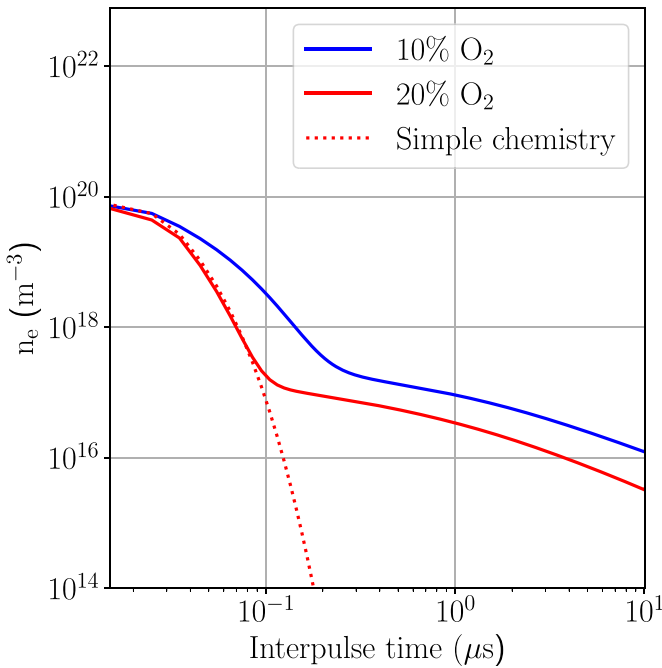


Figure 7. The temporal evolution of the electron density during the interpulse phase. The values were obtained at a point 1 mm below the electrode tip. The plot with ‘Simple chemistry’ will be elaborated further in section 4.4.

uncertainties in the 0D plasma-chemical modeling in [22], due to corrections to the scaling with pressure, and due to the different electrode geometries and pulse shapes. We therefore consider our results to be in relatively good agreement with [22].

In [18], experiments were performed in a 1 mm overvolted DBD gap containing N₂ with 0.1% O₂ at atmospheric pressure, and a 10 kV voltage was applied with a 10 kHz repetition frequency. Different breakdown regimes were observed by varying the voltage-off time t_{off} between pulses. For

$t_{\text{off}} > 20 \mu\text{s}$, a positive streamer propagated between the dielectric-covered electrodes, similar to the streamer repetition regime shown in figures 3 and 4. For $20 \mu\text{s} > t_{\text{off}} > 4 \mu\text{s}$, a slower and more diffuse positive streamer developed, which was attributed to a high residual electron density in the gap. Finally, for $t_{\text{off}} < 0.5 \mu\text{s}$ no streamer propagation occurred, and instead a re-ignition of the previous discharge’s afterglow was observed, similar to the inhibition regime shown in figures 3 and 4. The authors explain these regimes through 1D modeling, which correlates t_{off} with the background ionization density that is present at the start of the next pulse, similar to the present study. The fact that similar regimes were observed despite the rather different operating conditions shows that left-over ionization plays a generic role in repetitively pulsed discharges.

4.2. Criterion for streamer continuation

If the channel eventually becomes electrically screened during the second pulse, as illustrated in the evolution in figure 5, a high electric field will again form at its tip, from which a streamer can continue to grow. Whether streamer continuation occurs therefore depends on the remaining conductivity in the previous channel and on the duration of the second pulse. Below we derive a rough estimate for streamer continuation.

We approximate the previous channel at the start of the second pulse as a cylinder with radius R and electric conductivity σ , with a semi-spherical cap, in which the electric field is equal to the background field E_{bg} , see figure 8. The electric current in the channel is then initially given by

$$I_0 = \pi R^2 \sigma E_{\text{bg}}. \quad (4)$$

This current will decrease over time due to the screening of the background field. For simplicity, we assume that the accumulated charge at the end of the channel is given by

$$Q(\tau) = I_0 \tau, \quad (5)$$

Table 2. Major reactions that consume and produce electrons when the voltage is turned off. The full reaction set as specified in [35] and used throughout the paper contained 21 electron attachment and recombination reactions and 18 electron detachment reactions. Reaction R4 from [43] was included to account for field-dependent electron detachment. Note the rate of this reaction should depend on the O_2 concentration [43], but for simplicity we here use a single rate coefficient for both O_2 concentrations, as the rates are similar. T (K) and T_e (K) are gas and electron temperatures, respectively. T_e is computed as $T_e = 2\epsilon_e/3k_B$ with the mean electron energy ϵ_e obtained from BOLSIG+ [44]. The ‘simple chemistry’ added in figure 7 also consists of reactions R1, R3, and R4.

No.	Reaction	Reaction rate coefficient ($m^6 s^{-1}$ or $m^3 s^{-1}$)	Reference
Major electron-loss reactions			
R1	$e + O_2 + O_2 \rightarrow O_2^- + O_2$	$k_1(E/N)$	[31]
R2	$e + O_2 + N_2 \rightarrow O_2^- + N_2$	$k_2 = 10^{-43}$	[31]
R3	$e + O_4^+ \rightarrow O_2 + O_2$	$k_3 = 1.4 \times 10^{-12} (300/T_e)^{0.5}$	[36]
Electron-detachment reactions			
R4	$O_2^- + M \rightarrow e + O_2 + M$	$k_4 = 1.24 \times 10^{-17} \exp(-(\frac{179}{8.8+E/N})^2)$	[43]
R5	$O_2^- + O_2^*(b) \rightarrow e + 2O_2$	$k_5 = 3.60 \times 10^{-16}$	[36]
R6	$O_2^- + N_2^*(A) \rightarrow e + O_2 + N_2$	$k_6 = 2.10 \times 10^{-15}$	[36]
R7	$O_2^- + O(^3P) \rightarrow e + O_3$	$k_7 = 1.50 \times 10^{-16}$	[36]
R8	$O_2^- + N(^4S) \rightarrow e + NO_2$	$k_8 = 5 \times 10^{-16}$	[36]
R9	$O_3^- + O(^3P) \rightarrow e + 2O_2$	$k_9 = 3 \times 10^{-16}$	[36]

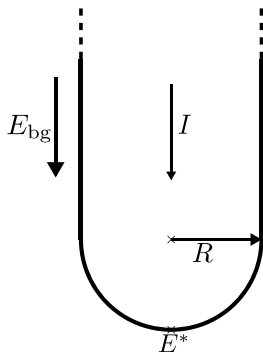


Figure 8. Schematic illustration of the assumed streamer shape used in section 4.2. The streamer is approximated by a cylinder with a hemispherical cap of radius R .

where τ is the time since the start of the second pulse. We assume this charge Q gives rise to an electric field similar to that of a (semi-)spherical charge distribution with radius R

$$E^*(\tau) = E_{bg} + \frac{1}{4\pi\epsilon_0} \frac{Q(\tau)}{R^2}. \quad (6)$$

If we now define a required electric field for discharge inception E_{inc} , we can determine the time τ it takes until $E^* = E_{inc}$. We include a correction factor k for this time scale, of order unity, which accounts for e.g. the partial screening over time and the fact that the actual channel is not a cylinder with a hemispherical cap. The resulting estimate for τ is then given by

$$\tau = 4k(E_{inc}/E_{bg} - 1)\tau_{drt}, \quad \text{where } \tau_{drt} = \epsilon_0/\sigma. \quad (7)$$

Equation (7) provides an estimate for the time τ needed for a streamer to emerge from the tip of a previous one (as illustrated in figure 5). Note that τ depends on the interpulse time through the conductivity σ , which decays in the previous channel during the interpulse time. We will now

compare equation (7) against the simulation results presented in section 3. We estimate the required field for discharge inception as $E_{inc} = 100 \text{ kV cm}^{-1}$. Since $E_{bg} = 15 \text{ kV cm}^{-1}$, the factor $4k(E_{inc}/E_{bg} - 1)$ is then about $23k$. In the simulations, we measure the time τ_{obs} until a field of strength E_{inc} has been reached at the tip of the previous streamer, with $\tau_{obs} = 0$ corresponding to the start of the second pulse plus its rise time of 1 ns. Furthermore, we approximate the effective conductivity of the previous streamer as

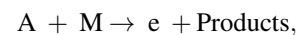
$$\sigma = \int_0^{R'} 2\pi r \sigma(r) dr / (\pi R'^2), \quad (8)$$

where $\sigma(r)$ is a radial conductivity profile 0.5 mm behind the streamer head, and R' is defined as the radius at which $\sigma(r)$ has dropped to 10% of its maximum value. Since the contribution of ions to the conductivity is relatively small for the cases considered here, we approximate $\sigma(r)$ as $e\mu_e(r)n_e(r)$.

In table 3, we list observed continuation times τ_{obs} together with $\tau_{drt} = \epsilon_0/\sigma$, where σ was computed according to equation (8) at the start of the second pulse. The ratio τ_{obs}/τ_{drt} lies between 24 and 38, which is in agreement with equation (7) for k between 1.0 and 1.5.

4.3. Role of detachment reactions

The chemistry we use [35] has 18 different electron detachment reactions which are of the form



where A is one of O^- , O_2^- , O_3^- and M is a neutral species in its ground or excited state.

Table 2 lists the six detachment reactions that contribute significantly to the production of electrons after the end of the first pulse. Although our chemistry includes electron detachment reactions from O^- ions, they are not included in table 3

Table 3. Dielectric relaxation times τ_{drt} at the start of the second pulse, based on equation (8), together with the observed inception delays τ_{obs} for second-pulse streamers. Specifically, τ_{obs} was here defined as the time it takes for the maximal electric field to reach 100 kV cm^{-1} after the rise time of the second pulse.

(a) 20% O ₂			
Δt_{inter} (ns)	τ_{drt} (ns)	τ_{obs} (ns)	$\tau_{\text{obs}}/\tau_{\text{drt}}$
10	0.0616	1.46	23.7
15	0.0978	2.86	29.2
20	0.162	4.88	30.1
25	0.267	7.01	26.3
50	—	—	—
(b) 10% O ₂			
Δt_{inter} (ns)	τ_{drt} (ns)	τ_{obs} (ns)	$\tau_{\text{obs}}/\tau_{\text{drt}}$
10	0.0349	1.11	31.8
15	0.0427	1.61	37.7
20	0.0553	2.05	37.1
25	0.0699	2.52	36.1
50	0.164	5.77	35.2

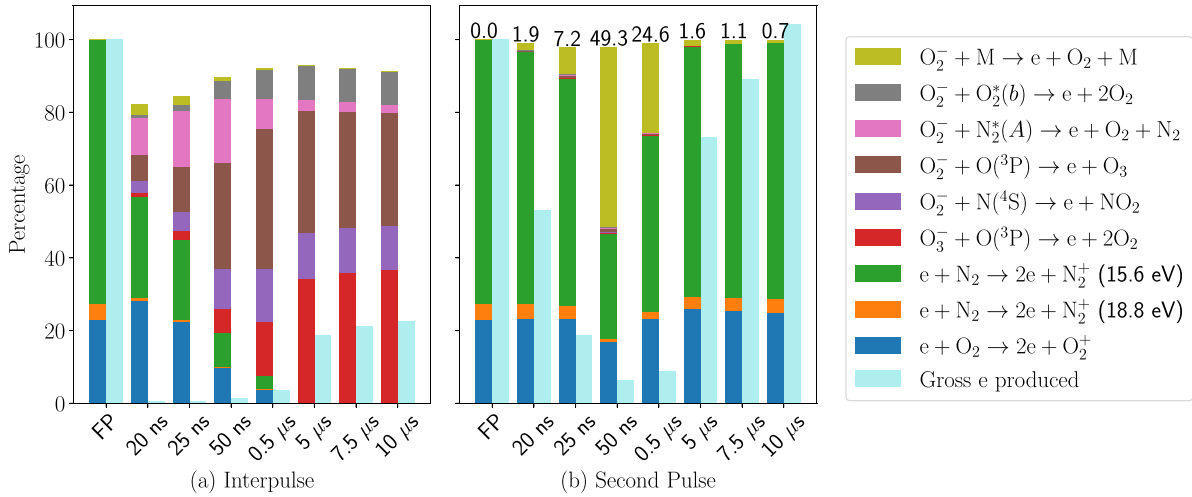


Figure 9. Relative contribution of electron-producing reactions during the interpulse (a) and the second pulse (b) for the case of 20% O₂. The production during the first pulse, and the gross electron production normalized with that of the first pulse is shown for comparison. The percentage contribution of the field dependent detachment reaction $\text{O}_2^- + \text{M}$ to the gross electron productions detachment is listed at the top of each bar in (b).

because they made a much smaller contribution for our operating conditions.

In figure 9(a) we show the relative contribution of electron-producing reactions during the interpulse for the case of 20% O₂. For short interpulse times, there is still a major contribution from ionization reactions, which take place due to the decaying field enhancement after the voltage is turned off. For longer interpulse times, most electron production is due to detachment reactions, with the relative contribution of O₃⁻ detachment increasing over time. Note that the reaction $\text{O}_2^- + \text{M} \rightarrow \text{e} + \text{O}_2 + \text{M}$ plays only a minor role during the interpulse due to its field-dependent rate coefficient.

Figure 9(b) shows relative contributions of electron-producing reactions during the second pulse. Now field-dependent detachment from O₂⁻ is the major electron detachment reaction. For Δt_{inter} equal to 50 ns and 500 ns, this reaction is responsible for a significant fraction of the total

electron production (which includes ionization reactions). This is mainly due to two factors: the availability of a large number of O₂⁻ ions, and a reduction in ionization reactions due to lower field enhancement in the inhibited growth regime, see figure 5(b). For interpulse times of 5 μs or more, O₂⁻ ions are lost due to negative-ion conversion and ion-ion recombination reactions. For interpulse times below 25 ns, detachment from O₂⁻ does not play a significant role since the previous channel is quickly screened and a new streamer forms.

Results for the case of 10% O₂ and 90% N₂ are given in appendix A. We observe a similar trend in the relative contributions of detachment reactions for this case.

4.4. Effect of using a different chemistry set

For comparison, we have also simulated the electron density decay during the interpulse with a simpler plasma chemistry

from [39]. This chemistry contains 8 species and 15 reactions, and it lacks the extensive electron, ion, neutral and excited species reactions as compared to the chemistry set used in the rest of this paper. For electrons, the same Phelps [31] cross sections are used. In figure 7, where we denote the smaller chemistry from this section as ‘Simple Chemistry’, we compare the electron decay inside the streamer channel during the interpulse phase. The decay agrees well up to 100 ns, but at later times the simpler chemistry predicts a much faster decay due to the absence of the various electron detachment reactions. For a pulse duration of 100 ns or more, the sets would therefore lead to different streamer continuation times.

5. Conclusions

We have investigated streamer continuation with double-pulse simulations in N_2 containing 20% and 10% O_2 at 1 bar. We use two identical voltage pulses of 15 ns, and vary the interpulse time Δt_{inter} between 5 ns and 10 μs . For increasing Δt_{inter} , we observe three regimes during the second pulse:

- In the streamer continuation regime ($\Delta t_{\text{inter}} \lesssim 50$ ns), a new streamer emerges from the tip of the previous one.
- In the inhibited growth regime (50 ns $\lesssim \Delta t_{\text{inter}} \lesssim 500$ ns, with somewhat longer time scales for 10% O_2), the previous channel is partially re-ionized, but there is considerable less field enhancement and almost no light emission. This re-ionization wave becomes stronger for increasing interpulse times, characterized by increased electric field screening and increased light emission.
- For $\Delta t_{\text{inter}} \gtrsim 5$ μs , a new streamer forms that is similar to the first one. However, even for the longest interpulse times considered here (10 μs) this new streamer has lower field enhancement and is less bright than the first one.

With 10% O_2 these regimes occurred at slightly longer interpulse times than with 20% O_2 , due to lower electron attachment and recombination rates.

In our simulations, streamer continuation occurred when the remaining electron density was in the range of 10^{19} m^{-3} up to $4 \times 10^{19} \text{ m}^{-3}$. This range agrees with the estimate made in [9], based on experimental measurements and 0D modeling, when scaled to the same pressure. We derived an estimate for the time needed for streamer continuation to occur which depends on the conductivity of the previous channel and the background electric field. This estimate and our observed values of streamer inception delay in the simulations are in reasonable agreement. Furthermore, we show that for interpulse times above 100 ns several electron detachment reactions significantly slow down the decay of the electron density.

6. Outlook

We obtained our current results using a specific background electric field, pulse shape and pressure. In future work, our

computational model could be improved in the following aspects:

- When the voltage falls to zero, the polarity of the electrode is reversed due to the remaining positive space charge. A cathode sheath with a really high local field is expected to form around the electrode, see e.g. [45–47]. Resolving such a sheath was computationally not feasible with our model, which is why homogeneous Neumann boundary conditions for species at the electrodes were used. The effect of more realistic electrode boundary conditions could be studied in future work.
- As shown in section 4.4, for longer interpulse times, it is important that we use a chemistry set that is complete and has accurate rate constants. It was also pointed out in [35] that some rate constants also depend on pressure and temperature. Thus, in order to be able to extend our results to different pressures, future work involves generalizing the reaction set.
- Finally, varying the pulse shape, background electric field, and gas composition might result in streamer branching, which would require fully 3D modeling.

These present and future investigations will allow for theoretical predictions for optimal pulse repetition frequencies for various plasma processing applications.

Data availability statements

The data that support the findings of this study are openly available at the following URL/DOI: <https://doi.org/10.5281/zenodo.8055893>.

Acknowledgments

This work was carried out on the Dutch national e-infrastructure with the support of SURF Co-operative. H M was supported by the STW-Project 15052 ‘Let CO_2 spark’. A M has received funding from the European Union’s Horizon 2020 research and innovation program under Project 722337 (SAINT). We thank Baohong Guo for his help with the plasma chemistry used in this paper.

Appendix A. Effect of varying O_2 concentration on detachment reactions

Here we show the relative contribution (in %) of various electron-producing reactions for the case of 10% O_2 . Figure A1 shows the contribution during the interpulse phase and figure A2 shows the contribution during the second pulse. In each of these figures, we also show the results from figure 9 for comparison.

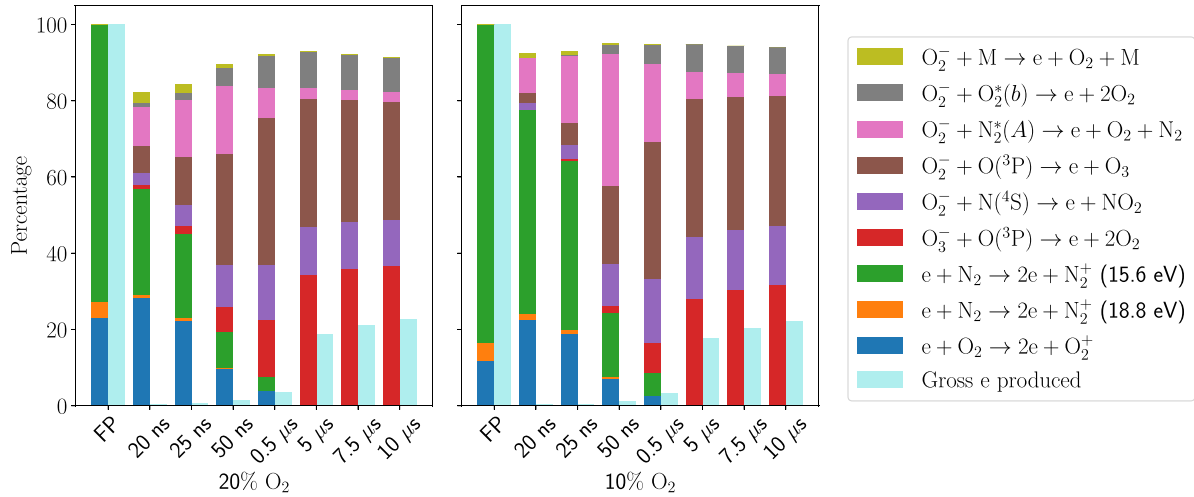


Figure A1. Relative contribution of electron-producing reactions during the interpulse for 10% O₂. The production during the first pulse is shown for comparison. We also show the gross electron production normalized to that of the first pulse.

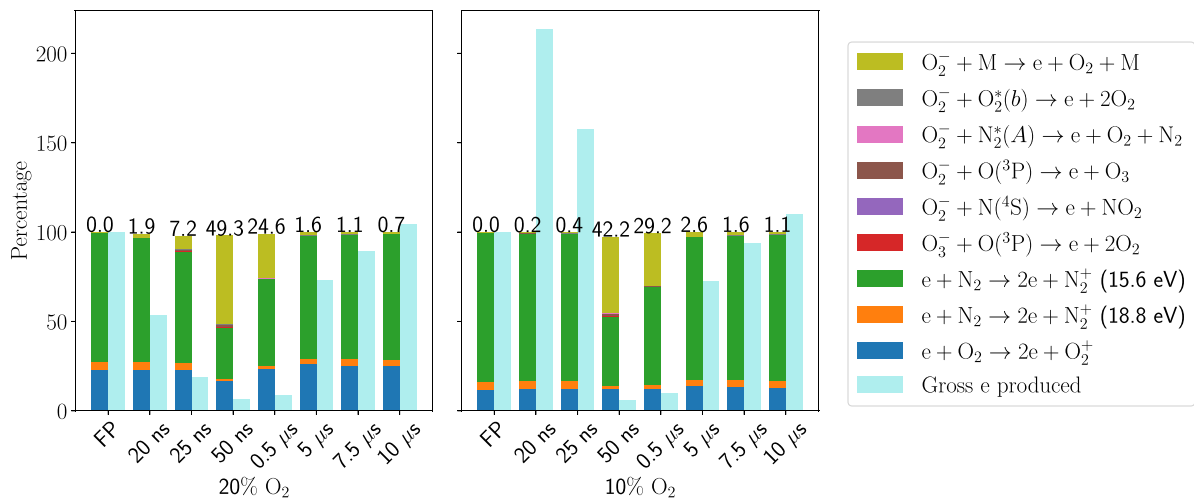


Figure A2. Relative contribution of electron-producing reactions during the second pulse for 10% O₂. The production during the first pulse and the gross electron production normalized to that of the first pulse is also shown. The percentage contribution of the field-dependent detachment reaction $O_2^- + M$ to the gross electron productions detachment is listed at the top of each bar plot. For 10% O₂ and $\Delta t_{\text{interp}} = 20$ ns and $\Delta t_{\text{interp}} = 25$ ns, gross electron production during the second pulse is higher than during the first pulse.

Appendix B. Electric field inside the streamer channel during the interpulse

In figure B1, we show the electric field decay over time at various locations along the axis of the streamer channel for 20% O₂. The electric field decays from 10^6 V m⁻¹ (41 Td) to 10^2 V m⁻¹ (0.004 Td) over a time interval of $5 \mu\text{s}$. However, the boundary conditions at the electrode are currently not very realistic in our model: a Neumann zero condition is used for electrons, which results in electrons freely entering the domain after the voltage is turned off. This leads to a faster decay of the

residual charge (and thus also of the electric field) than would occur with more realistic boundary conditions.

In principle it is possible to specify more realistic boundary conditions at the electrode, in which the outflow of electrons is caused by secondary emission processes. However, with such boundary conditions we cannot run simulations for long time scales, since the anode effectively becomes a cathode after the voltage is turned off, resulting in the formation of thin sheaths with very high local electric fields. We intend to improve our model's boundary conditions in the future, for example by using the local energy approximation as in [48] and/or by approximating the electron dynamics in the sheath.

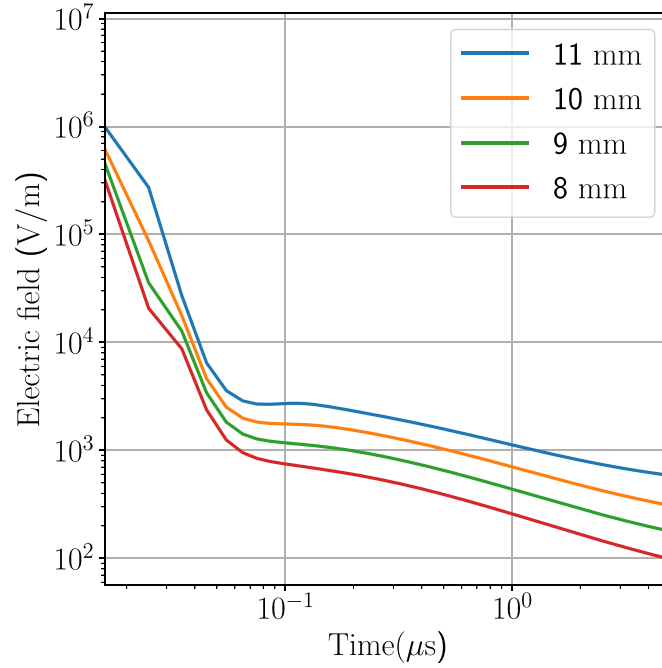


Figure B1. The temporal evolution of the on-axis electric field inside the streamer channel during the interpulse phase. The values were obtained at points 1, 2, 3 and 4 mm below the electrode tip, which is approximately located at $z = 12$ mm.

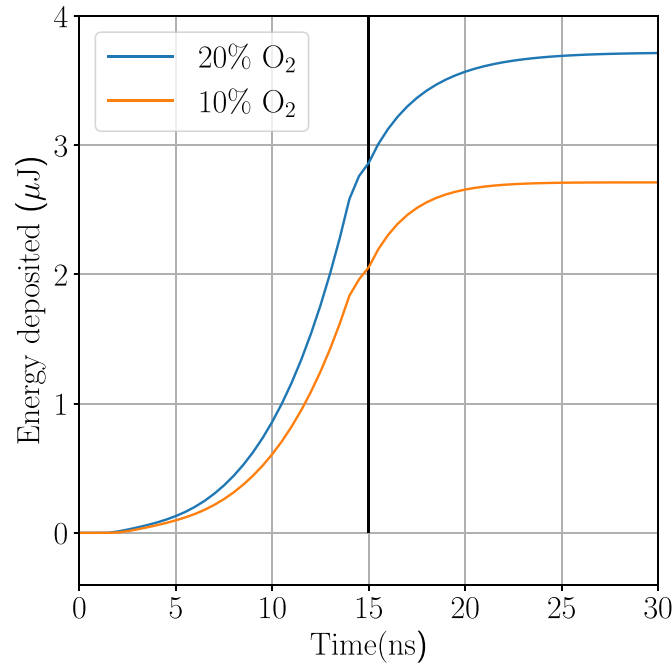


Figure C1. Space-time integrated Joule heating term. The vertical line is at the 15 ns mark, where the first pulse is turned off.

Appendix C. Effect of gas heating

Figure C1 shows the space-time integrated Joule heating ($\vec{j} \cdot \vec{E}$) during the first pulse. The energy deposited due to the first pulse is below $4 \mu\text{J}$, and no energy is deposited after 25 ns. At 1 bar and 300 K, dry air (80% N_2 :20% O_2) has a density $\rho = 1.2 \text{ kg m}^{-3}$ and a specific heat capacity $C_p = 1000 \text{ J kg}^{-1} \text{ K}^{-1}$. This energy is deposited in a cylindrical volume of radius $r = 0.8$ mm (maximum width of the

streamer channel) and height $h \approx 5.5$ mm (first pulse streamer length). Even if we assume that all the energy instantaneously goes into gas heating, the temperature increase is only about $\Delta T = 4 \mu\text{J} / (C_p \rho \pi r^2 h) \approx 0.3$ K. Such a small increase in temperature will not have a significant effect on the second-pulse streamer properties, which is why gas heating was not included in our model. In a follow-up paper that is in preparation, we are exploring the effects of gas heating after many pulses.

ORCID iDs

H Malla  <https://orcid.org/0000-0002-9737-8223>
 A Martinez  <https://orcid.org/0000-0002-7826-2348>
 U Ebert  <https://orcid.org/0000-0003-3891-6869>
 J Teunissen  <https://orcid.org/0000-0003-0811-5091>

References

- [1] Vitello P, Penetrante B and Bardsley J 1994 *Phys. Rev. E* **49** 5574
- [2] Nijdam S, Teunissen J and Ebert U 2020 *Plasma Sources Sci. Technol.* **29** 103001
- [3] Verloy R, Privat-Maldonado A, Smits E and Bogaerts A 2020 *Cancers* **12** 2782
- [4] Graves D B 2014 *Phys. Plasmas* **21** 080901
- [5] Laroussi M 2014 *Plasma Process. Polym.* **11** 1138–41
- [6] Ranieri P, Sponsel N, Kizer J, Rojas-Pierce M, Hernández R, Gatiboni L, Grunden A and Stapelmann K 2021 *Plasma Process. Polym.* **18** 2000162
- [7] Bárdos L and Baránková H 2010 *Thin Solid Films* **518** 6705–13
- [8] Starikovskaia S M 2006 *J. Phys. D: Appl. Phys.* **39** R265
- [9] Nijdam S, Takahashi E, Markosyan A H and Ebert U 2014 *Plasma Sources Sci. Technol.* **23** 025008
- [10] Li Y, Van Veldhuizen E M, Zhang G J, Ebert U and Nijdam S 2018 *Plasma Sources Sci. Technol.* **27** 125003
- [11] Mirpour S, Martinez A, Teunissen J, Ebert U and Nijdam S 2020 *Plasma Sources Sci. Technol.* **29** 115010
- [12] Pai D Z, Lacoste D A and Laux C O 2010 *J. Appl. Phys.* **107** 093303
- [13] Tholin F and Bourdon A 2013 *Plasma Sources Sci. Technol.* **22** 045014
- [14] Lu X and Ostrikov K 2018 *Appl. Phys. Rev.* **5** 031102
- [15] Chang L, Nie L, Xian Y and Lu X 2016 *Phys. Plasmas* **23** 123513
- [16] Babaeva N Y, Naidis G, Tarasenko V, Sorokin D, Zhang C and Shao T 2022 *Plasma Sci. Technol.* **25** 035406
- [17] Höft H, Kettlitz M, Weltmann K and Brandenburg R 2014 *J. Phys. D: Appl. Phys.* **47** 455202
- [18] Höft H, Kettlitz M, Becker M, Hoder T, Loffhagen D, Brandenburg R and Weltmann K 2014 *J. Phys. D: Appl. Phys.* **47** 465206
- [19] Zhao Z, Huang D D, Wang Y N, Li C J and Li J T 2020 *Plasma Sources Sci. Technol.* **29** 015016
- [20] Zhao Z, Li C, Guo Y, Zheng X, Sun A and Li J 2023 *Plasma Sources Sci. Technol.* **32** 015002
- [21] Zhao Z and Li J 2020 *High Volt.* **5** 569–82
- [22] Nijdam S, Takahashi E, Teunissen J and Ebert U 2014 *New J. Phys.* **16** 103038
- [23] Nijdam S, Teunissen J, Takahashi E and Ebert U 2016 *Plasma Sources Sci. Technol.* **25** 044001
- [24] Pancheshnyi S 2005 *Plasma Sources Sci. Technol.* **14** 645
- [25] Naidis G 2011 *J. Phys. D: Appl. Phys.* **44** 215203
- [26] Teunissen J and Ebert U 2017 *J. Phys. D: Appl. Phys.* **50** 474001
- [27] Li X, Dijkcs S, Nijdam S, Sun A, Ebert U and Teunissen J 2021 *Plasma Sources Sci. Technol.* **30** 095002
- [28] Wang Z, Sun A and Teunissen J 2022 *Plasma Sources Sci. Technol.* **31** 015012
- [29] Bagheri B et al 2018 *Plasma Sources Sci. Technol.* **27** 095002
- [30] Hagelaar G J M and Pitchford L C 2005 *Plasma Sources Sci. Technol.* **14** 722–33
- [31] Phelps database (available at: www.lxcat.net) (Accessed 19 August 2021)
- [32] Zhelezniak M B, Mnatsakanian A K and Szykh S V 1982 *High Temp. Sci.* **20** 357–62 (available at: <https://ui.adsabs.harvard.edu/abs/1982HTemS..20..357Z/abstract>)
- [33] Teunissen J and Ebert U 2018 *Comput. Phys. Commun.* **233** 156–66
- [34] Teunissen J and Schiavello F 2023 *Comput. Phys. Commun.* **286** 108665
- [35] Guo B and Teunissen J 2023 *Plasma Sources Sci. Technol.* **32** 025001
- [36] Kossyi I A, Kostinsky A Y, Matveyev A A and Silakov V P 1992 *Plasma Sources Sci. Technol.* **1** 207–20
- [37] Ono R and Komuro A 2020 *J. Phys. D: Appl. Phys.* **53** 035202
- [38] Tochikubo F and Arai H 2002 *Jpn. J. Appl. Phys.* **41** 844
- [39] Li X, Guo B, Sun A, Ebert U and Teunissen J 2022 *Plasma Sources Sci. Technol.* **31** 065011
- [40] Pancheshnyi S, Nudnova M and Starikovskii A 2005 *Phys. Rev. E* **71** 016407
- [41] Hansen E W and Law P L 1985 *J. Opt. Soc. Am. A* **2** 510–20
- [42] Aleksandrov N L and Bazelyan E M 1999 *Plasma Sources Sci. Technol.* **8** 285–94
- [43] Pancheshnyi S 2013 *J. Phys. D: Appl. Phys.* **46** 155201
- [44] Bolsig+ (linux) 2019 (available at: <http://www.bolsig.laplace.univ-tlse.fr/>)
- [45] Odrobina I and Černák M 1995 *J. Appl. Phys.* **78** 3635–42
- [46] Babaeva N Y 2015 *Plasma Sources Sci. Technol.* **24** 034012
- [47] Yan W, Liu F, Sang C and Wang D 2014 *Phys. Plasmas* **21** 013504
- [48] Jovanović A P, Loffhagen D and Becker M M 2022 *Plasma Sources Sci. Technol.* **31** 04LT02